

---

This is the **accepted version** of the article:

Navarro Senent, Cristina; Pané, Salvador; Sort Viñas, Jordi; [et al.]. «The order of addition and time matters: Impact of electrolyte processing on micelle-assisted electrosynthesis of mesoporous alloys». *Electrochimica Acta*, Vol. 358 (October 2020), art. 136940. DOI 10.1016/j.electacta.2020.136940

---

This version is available at <https://ddd.uab.cat/record/233365>

under the terms of the  license

# The order of addition and time matters: impact of electrolyte processing on micelle-assisted electrosynthesis of mesoporous alloys

Cristina Navarro-Senent,<sup>a,\*</sup> Salvador Pané,<sup>b</sup> Jordi Sort<sup>a,c</sup> and Eva Pellicer<sup>a,\*\*</sup>

<sup>a.</sup> Departament de Física, Facultat de Ciències, Universitat Autònoma de Barcelona E-08193 Bellaterra (Cerdanyola del Vallès), Barcelona, Spain.

<sup>b.</sup> Institute of Robotics and Intelligent Systems, Swiss Federal Institute of Technology ETH Zurich, Tannenstraße 3, 8092 Zurich, Switzerland.

<sup>c.</sup> Institució Catalana de Recerca i Estudis Avançats (ICREA), Pg. Lluís Companys 23, E-08010 Barcelona, Spain.

\* To whom correspondence should be addressed:

\* [Cristina.Navarro.Senent@uab.cat](mailto:Cristina.Navarro.Senent@uab.cat)

\*\* [Eva.Pellicer@uab.cat](mailto:Eva.Pellicer@uab.cat)

**Keywords:** electrodeposition; mesoporous alloys; cobalt-platinum; amphiphilic surfactant

## Abstract

Mesoporous thin films are currently awaking a considerable interest for their prospective use in applications ranging from catalysis to energy storage applications. Yet, some of the synthetic parameters enabling a reproducible development of mesoporosity remain uncontrolled. In this research, we demonstrate that a subtle change in the procedure for the electrolyte preparation for the electrosynthesis of mesoporous Co–Pt films is critical for reproducing the mesoporosity of the alloys. Specifically, we show that dissolution of the platinum salt ( $\text{Na}_2\text{PtCl}_6 \cdot 6\text{H}_2\text{O}$ ) in water and storage of the solution (referred to as ‘equilibration time’) before adding the remaining reagents and additives ( $\text{CoCl}_2$  and P-123) are imperative to consistently reproduce the films mesoporosity. Highly mesoporous Pt-rich Co–Pt films (10-23 at.% Co), with a pore diameter of 10–17 nm, were obtained from an electrolyte that involved an equilibration time, while mesoporosity was often absent in films grown from a freshly prepared electrolyte (i.e., upon dissolving all chemicals immediately before electrodeposition). The results suggest that pore formation is governed by the complexation dynamics of Pt(IV) in water, which was investigated by UV-Vis spectroscopy. Namely, the concentration of hydroxochloroplatinate complexes ( $[\text{PtCl}_{6-x}(\text{OH})_x]^{2-}$ ) originating from the exchange of  $\text{Cl}^-$  by  $\text{OH}^-$  ions increase during the equilibration time.  $[\text{PtCl}_{6-x}(\text{OH})_x]^{2-}$  species would interact more favorably with the hydrophilic poly(ethylene oxide) moieties of P-123 micelles than  $[\text{PtCl}_6]^{2-}$ . The distinct interaction between micelles and the complexes of platinum is key for the reproducible generation of a mesoporous network. Our finding highlights the relevant role of electrolyte processing for the control of mesoporosity in metallic systems prepared by micelle-assisted electrodeposition, which we believe can be extended to many electrolytic processes.

## 1. Introduction

Mesoporous metals and alloys have been increasingly engaging researchers during the last decade for their prospective use as critical building blocks in a wealth of applications including energy conversion, sensing, or information technologies [1,2]. Apart from exhibiting pore sizes in the range from 2 nm to 50 nm, mesoporous metals and alloys are distinguished from other mesoporous matter with high electrical and thermal conductance. Furthermore, the porous architecture can be conveniently tailored to fine-tune specific features or develop new effects. Typical processes for the synthesis of mesoporous metallic matter are hard-templating, soft-templating or solution-phase approaches [3]. The use of soft templates such as lyotropic liquid crystals [4] and micelle assemblies have become prevalently widespread in the last few years.

Micelle assemblies were first exploited by Yamauchi and co-workers in their seminal paper describing the electrodeposition of platinum metal from diluted (1.0 wt %) non-ionic surfactant solutions [5]. The procedure was later extended to Pd [6] and bimetallic systems such as PtPd [7], PtRu [8] and PtAu [9]. Recently, our group showed that the production of high-quality mesoporous films comprising a noble metal (Pt) and a transition non-noble metal (e.g., Ni, Fe and Co), in a partially or fully alloyed state, is also feasible [10-12].

Among all methods to produce mesoporous metals and metallic alloys via soft templating, electrochemical deposition is a suitable technique to reduce the metal ions in a solution [3]. Different non-ionic surfactant assemblies have been used so far, like the commercial P-123 and F-127 Pluronics, Brij 58, as well as surfactants obtained by in-house synthesis, always above their critical micelle concentration. In addition, electrochemical deposition allows for an spatiotemporal control over the growth of matter when

electrochemical processes are forced to occur in confinement, i.e. in the porous channels of nanotemplates, or in microarrays obtained by photolithography [13,14].

While several striking outcomes have been demonstrated with electrochemical deposition, the belief that this technique is a sort of potion making, where additives are magic ingredients, persists. However, note that, despite the maturity of the technique, the synergistic role of additives in electrochemical deposition is still a largely unexplored facet. Systematic studies devoted to formulations for electroplating are scarce. For example, an often-overlooked aspect is the effect of solution preparation and handling prior to electrodeposition on the properties of the deposited material. Frequently, electrodeposition is carried out immediately after electrolyte preparation (referred to as ‘freshly prepared electrolyte’) [15-17]. Here, we noticed that, during a series of unrelated experiments regarding the electrodeposition of mesoporous alloys, the mixing order of reagents and the time elapsed between electrolyte preparation and the actual electrodeposition, was critical for the reproducibility of the final mesostructure.

Considering that reliability is fundamental for the maturity of the technology and its translation to upscaled industrial processes, here we assess the influence of electrolyte processing on the quality of mesoporous films fabricated by electrochemical deposition. Essentially, we attempt to capture the conditions that ensure homogeneous mesoporosity over the entire film surface in successive depositions or in depositions performed in different days. The Co–Pt system is selected as a case study for this purpose for several reasons. First, mesoporous Co–Pt films can be grown by electrodeposition from P-123 micelle assemblies [12]. Secondly, Co–Pt exhibits several interesting functionalities, as an electrocatalyst [18], or in magnetic microelectromechanical

applications [19]. More recently, magnetoelectric effects in porous Co–Pt materials for potential use in spintronic devices have also been reported [12].

Our results indicate that the electrolytes can behave as dynamic systems, in which the order of addition and time can dramatically impact the behavior of an electrochemical process. In the presented case, prior dissolution of the platinum salt in water followed by a storage period before addition of the remaining chemicals is essential for the reproducible formation of the mesostructure during electrocrystallization. The use of freshly prepared electrolytes is discouraged since in this case the occurrence of controlled mesoporosity is elusive.

## **2. Experimental**

### *2.1 Materials*

Isopropyl alcohol ( $\text{C}_3\text{H}_8\text{O}$ , 99.9%), acetone (99.0%),  $\text{Na}_2\text{PtCl}_6 \cdot 6\text{H}_2\text{O}$  (sodium hexachloroplatinate (IV) hexahydrate, 98.0%),  $\text{CoCl}_2$  (cobalt(II) chloride anhydrous,  $\geq 98.0\%$ ), Pluronic P-123 ( $\text{HO}(\text{CH}_2\text{CH}_2\text{O})_{20}(\text{CH}_2\text{CH}(\text{CH}_3)\text{O})_{70}(\text{CH}_2\text{CH}_2\text{O})_{20}\text{H}$ ) block copolymer, and HCl (hydrochloric acid, 37 wt.%) were purchased from Sigma-Aldrich. All reagents were used as received without further purification. Deionized water was obtained through an EMD Millipore Simplicity™ Water Purification.

### *2.2 Instrumentation*

Electrodeposition was performed in a one-compartment thermostated three-electrode cell connected to a PGSTAT302N Autolab potentiostat/galvanostat (Metrohm-Autolab). A double junction  $\text{Ag}|\text{AgCl}$  ( $E = +0.210 \text{ V/SHE}$ ) reference electrode was used with 3 M potassium chloride (KCl) inner solution and 1 M sodium chloride (NaCl) outer solution.

A platinum spiral was used as counter electrode. Silicon chips with sputtered titanium (20 nm)/copper (200 nm) adhesion/seed layers were employed as working electrodes. The chip backside was made of SiO<sub>2</sub> to avoid electrodeposition on both sides. The platable area was  $0.25 \pm 0.01 \text{ cm}^2$ . For cyclic voltammetry (CV) studies, a vitreous carbon rod (Metrohm) of  $0.0314 \text{ cm}^2$  served as the working electrode. A single cycle was run with a lower limit of  $-1.3 \text{ V}$  and an upper limit of  $1.0 \text{ V}$  vs. Ag|AgCl, at a scan rate of  $50 \text{ mV s}^{-1}$ . The potential was initially swept toward cathodic values starting from a value in which no current was recorded.

### *2.3 Electrode preparation and films growth*

Prior to deposition, the metallized Si chips were cleaned with acetone and isopropanol, rinsed with Milli-Q water and dried with N<sub>2</sub>. Deposition was conducted potentiostatically at potentials between  $-0.9$  and  $-1.1 \text{ V}$  (for Baths 1, 3 and 4) and between  $-1.0$  and  $-1.4 \text{ V}$  (for Bath 2) during 600 s (**Table 1**). Deposition was carried out under mild stirring ( $\omega = 100 \text{ rpm}$ ) while simultaneously bubbling N<sub>2</sub> through the solution. The temperature was set at  $25 \text{ }^\circ\text{C}$  by making water circulate throughout the external jacket of the electrochemical cell by means of an F12 Julabo thermostat. After electrodeposition, the samples were rinsed in slightly acidic water followed by Milli-Q water and dried with argon gas.

### *2.4 Morphology and structural characterization*

Deposit morphology and porosity was examined by field emission scanning electron microscopy (FE-SEM) on a Zeiss MERLIN operated at 5kV. The elemental composition was determined by Energy Dispersive X-ray Spectroscopy (EDXS) at an acceleration voltage of 15 kV. ImageJ processing software was used to determine the pore size distribution in the

Co–Pt films from their on-top surfaces. The crystallographic structure was examined by X-ray diffraction (XRD). XRD patterns were recorded on a Philips X'Pert diffractometer using  $K_{\alpha}$  radiation. Diffractograms were recorded in the  $38\text{--}63^{\circ}$   $2\theta$  range with a step time of 8 s and a step size of  $0.026^{\circ}$ . The mean crystallite size was calculated from the XRD patterns by applying the Scherrer's formula on the peak's width. For film thickness determinations, samples were cut mechanically using a diamond tip to be able to observe and measure the cross-sections of Co-Pt films by FESEM.

### *2.5 Study of Pt(IV) complexes evolution with time*

UV-Vis spectroscopy was carried out on an HP8453 spectrophotometer (Hewlett-Packard). The evolution of  $[\text{PtCl}_6]^{2-}$  complex in water with time was studied on a 0.0039 M  $\text{Na}_2\text{PtCl}_6 \cdot 6\text{H}_2\text{O}$  aqueous solution. The UV-Vis transmittance spectra were recorded from 300 to 700 nm at different time intervals.

## **3. Results and discussion**

### *3.1 Electrolyte design and handling*

Co–Pt films were prepared by electrodeposition from solutions containing  $\text{Na}_2\text{PtCl}_6 \cdot 6\text{H}_2\text{O}$ ,  $\text{CoCl}_2$ , and Pluronic P-123. Four electrolytes were prepared in which the 'equilibration time' was either implemented or not and the concentration of  $\text{CoCl}_2$  was varied (**Table 1**). We define the 'equilibration time' as the period of time (10 days) that elapses between the dissolution of  $\text{Na}_2\text{PtCl}_6 \cdot 6\text{H}_2\text{O}$  (or  $\text{Na}_2\text{PtCl}_6 \cdot 6\text{H}_2\text{O} + \text{P-123}$ ) in water and the addition of the other chemicals, after which electrodeposition is immediately carried out. A 10-day storage was chosen as optimum "equilibration time" in order to ensure a



steady-state and avoid transitory effects. For Baths 1 and 3, an aqueous solution of  $\text{Na}_2\text{PtCl}_6 \cdot 6\text{H}_2\text{O}$  was prepared and stored for 10 days, followed by the addition of Pluronic P-123 and  $\text{CoCl}_2$  in that order (**Figure S1a** and **S1c**). The concentration of  $\text{CoCl}_2$  was 10 times higher in Bath 3 compared to Bath 1 (**Table 1** and **Figure S1c**). For Bath 2, an aqueous solution of  $\text{Na}_2\text{PtCl}_6 \cdot 6\text{H}_2\text{O}$  was prepared, immediately followed by the addition of Pluronic P-123 and  $\text{CoCl}_2$ , without introducing an 'equilibration time' (**Figure S1b**). Finally, a solution containing  $\text{Na}_2\text{PtCl}_6 \cdot 6\text{H}_2\text{O}$  and Pluronic P-123 was prepared and stored for 10 days, after which  $\text{CoCl}_2$  was added (**Figure S1d**). The pH was adjusted to 2.3 with the addition of a few drops of HCl 1 M in all cases. The concentration of Pluronic P-123 surfactant and  $\text{Na}_2\text{PtCl}_6 \cdot 6\text{H}_2\text{O}$  was 1 wt.% ( $1 \text{ mg mL}^{-1}$ ) and 0.0013 M, respectively, in all electrolytes (**Table 1**). The concentration of P-123 was above its critical micelle concentration (c.m.c.) at 25 °C [20] in order to ensure the formation of micelles in the electrolyte.

In the micelle-assisted electrodeposition process, the metallic ions, which are coordinated by the hydrophilic shell domain of the P-123 micelles, migrate toward the working electrode (**Steps 1 and 2, Figure 1**). Once they reach the cathode, Pt(IV) and Co(II) cations are reduced (**Step 3, Figure 1**), which results in the formation of a mesoporous Co–Pt film (**Step 4, Figure 1**). Therefore, the purpose of this approach is to exploit the self-assembly of P-123 molecules into micelles which gather spontaneously at the solid–liquid interface during the electrodeposition of the mesoporous Co–Pt film.

### 3.2 Cyclic voltammetry study

Cyclic voltammetry (CV) curves from different electrolytes were recorded, aimed at gathering information on the influence of the equilibration time on the redox processes

taking place (**Figure 2** and **Figure 3**). As seen in **Figure 2**, Bath 2 is characterized by a weak reduction wave around  $-0.3$  V corresponding to platinum deposition [21], followed by a sharp increase of the current at more negative potentials. This sharp increase of the reduction current can be ascribed to hydrogen evolution which superimposes with the codeposition of Co as the scan proceeds. The potential at which current density rapidly increases is different in Baths 1 and 2. Namely, a shift of  $0.3$  V towards more positive values is observed for Bath 1 (inset of **Figure 2**). This was an unexpected result since bath formulation and pH were identical and suggests that the equilibration time introduced in Bath 1 favors Pt deposition. As the potential is swept toward more negative values, two reduction peaks located at  $-0.67$  V and  $-0.89$  V are clearly observed in Bath 1, whereas they nearly overlap in Bath 2. In the anodic scan, a double oxidation peak centered at  $-0.3$  V is detected in both cases, followed by a weaker peak around  $+0.75$  V. The double peak is related to the oxidation of Co–Pt alloy with varying Pt/Co ratio, whereas the second weaker peak is presumably related to the oxidation of Pt [21]. The oxidation charge under the right side of the double oxidation peak is higher in Bath 2 compared to Bath 1, suggesting that the discharge of Co(II) relative to Pt(IV) increased during the cathodic scan from Bath 2.

The electrochemical fingerprint of Baths 1 and 3 can be compared in **Figure 3**. Again, a shift in the potential value from which the reduction current rapidly increases is observed. This shift, however, is much less pronounced (around  $0.1$  V) and can be attributed to the change in concentration of Co(II) salt, which is 10 times higher in Bath 3. Yet, the deposition onset is detected at a more positive potential for Bath 3 compared to Bath 2 (cf. green curve in **Figure 3** and blue curve in **Figure 2**). In the anodic scan, the charge under the right side of the double oxidation peak increases drastically, indicating the

formation of a deposit much richer in Co in the reduction zone. According to the information acquired from the CV study, a range of potentials suitable for the potentiostatic deposition of the Co–Pt films on Cu was chosen (Figure S2). As such, differences among the deposits resulting from the various baths were anticipated.

### *3.3 Morphology, porosity, and composition of the films*

**Figure 4** shows field-emission scanning electron microscopy (FE-SEM) images of the mesoporous Co–Pt thin films prepared from Bath 1 at different potentials. As shown in **Figure 4a–c**, nanometer-sized pores are visible all over the surface of the films. Furthermore, the morphology and porosity were almost independent from the applied potential. Pore size was measured from the high-magnification SEM images, and the corresponding pore size distributions are shown in **Figure 4d–f**. Pore diameters were in the range of 13–17 nm for films deposited at –0.9 V and –1.0 V, with the majority of pores having diameters of 15 nm and 14 nm, respectively (**Figure 4d** and **e**). Films deposited at –1.1 V featured pore diameters in the range of 10–14 nm with a maximum at 12 nm (**Figure 4f**). In contrast, Co–Pt thin films electrodeposited from Bath 2 show a completely different morphology (**Figure 5**). The applied potentials were negatively shifted according to the  $\Delta E$  previously observed in the CVs (**Figure 2**) in order to obtain similar current densities (**Figure S2**). Thin films deposited at –1.2V showed rounded grains (**Figure 5a**), while films deposited at –1.3 and –1.4 V consisted of elliptical/acicular grains (**Figure 5b** and **c**). This transformation from rounded to acicular/elliptical shape suggest an increase of the Co content in the films. Note that this acicular morphology has often been reported in electrodeposited Co-rich Co based alloys [22,23]. In addition, an effect of the potential

on the grain size is observed, where smaller grains were obtained at more positive potentials. More importantly, most of the specimens deposited from Bath 2 did not display a clear mesoporosity (Figure 5). A mesoporous network occasionally developed in samples produced from some batches and it was clear that Bath 2 lacked reproducibility. For this electrolyte, porosity is developed at more positive potentials, although deposit morphology was distinct from that observed in the films obtained from Bath 1 (**Figure S3**). The morphology of the deposit grown at  $-1.1$  V (**Figure S3b**), characterized by rounded grains with nanometer-sized pores in a cauliflower fashion, displayed a mixture of morphologies between those observed at  $-1.0$  and  $-1.2$  V (Figure S3a and Figure 5a respectively). Such intermingling morphology was probably due to the concomitant influence of applied potential and thickness (Table S1, Supporting Information). Note that the film deposited from Bath 1 at  $-1.1$  V (23 at.% Co) and the film obtained from Bath 2 at  $-1.0$  V (20 at.% Co) were compositionally alike, and yet they were morphologically different. Furthermore, films from Bath 2 showed a sort of edge effect characterized by a darkening of the deposit color toward the edges, which was visible at naked eye. This effect was also observed in films obtained from Bath 1 but to a much lesser extent (**Table 2**). A change in morphology was detected by SEM while imaging two different regions of the films produced from Bath 2 (**Figure S4a and b**). The thickness of the films correlated nicely with the increase in the deposition charge as the applied potential was made more negative (**Table S2**). While for Bath 1 there was not a significant change in deposit morphology and pore topology with the applied potential and thickness (77-160 nm), the situation was different for Bath 2 (90-250 nm).

Elemental composition analysis by Energy Dispersive X-ray Spectroscopy (EDX) revealed an increase of the cobalt content in the deposits produced from a fixed bath as

the applied potential was made more negative (**Table 2**), which is in agreement with the CV data. Interestingly, the films deposited from Bath 1 showed comparatively lower cobalt contents than the deposits from Bath 2 (**Table 2**). This result, together with the elusive generation of porosity in the latter, suggested that the presence of a high content of platinum in the films was strongly correlated to the building of an extended mesoporosity. Such correlation has been drawn in previous studies, in which proper interaction between noble metal ions of Pt and Pd and the block-copolymer micelles (Step 1, **Figure 1**) is known to favor the formation of a long-range order mesostructured [6,24].

In order to determine whether the occurrence of porosity in the deposits from Bath 1 was due to their higher Pt content or the equilibration time introduced during the electrolyte preparation, the Co(II) concentration in the electrolyte was increased by 10-fold (Bath 3, **Table 1**). Surprisingly, the resulting films showed a Co-rich like morphology combined with a mesoporous structure (**Figure 6**), which was different from that observed in deposits from Bath 1 (**Figure 4**). Importantly, the development of mesoporosity was fully reproducible unlike depositions from Bath 2. Moreover, deposits were dark grey with no apparent color gradient throughout their surface (**Table 2**). As for the films from Bath 2 (**Figure 5**), a change from clustered rounded grains to clustered needles was observed as the potential was made more negative (**Figure 6a and c**). This anticipated, again, an increase of the cobalt content. Indeed, cobalt amount was 5 at.% higher than in deposits from Bath 2 (see **Table 2**), thus confirming that the origin of mesoporosity in Bath 1 derived films can be ascribed to electrolyte processing and not to the Co/Pt ratio in the film. Therefore, it can be concluded that the equilibration time of Pt(IV) salt in water endows films with a reproducible mesoporosity.

Finally, the electrolyte was processed following a different procedure, in which  $\text{Na}_2\text{PtCl}_6 \cdot 6\text{H}_2\text{O}$  was dissolved together with P-123 (Bath 4, **Table 1**) in water and stored for 10 days before  $\text{CoCl}_2$  was added. Thin films obtained from this bath consistently showed in consecutive depositions a flat morphology and mesoporosity analogous to those of deposits obtained from Bath 1 (**Figure 4**), although with narrower pores (Figure S5). Similarly, EDX analyses revealed an elemental composition close to deposits from Bath 1, with a difference of just 5 at.% in Co (c.f. Baths 1 and 4, **Table 2**). The results suggest that the addition of P-123 during the equilibration time step does not induce significant changes on the morphology, porosity and composition of the deposits. Thus, it can be concluded that the reproducible formation of the mesoporous network is ruled by the dynamics of Pt(IV) complexes. In other words, prior dissolution of the Pt salt and storage of the solution greatly controls the mesoporosity of the films.

### 3.4 Crystallographic structure

X-Ray diffraction (XRD) analyses were performed to determine the crystallographic phases of the Co–Pt films prepared from Baths 1, 2 and 3 (**Figure 7a, b and c** respectively). For deposits grown from Bath 1, the main peaks located at  $40.5^\circ$  and  $47.15^\circ$  match the face-centered cubic (fcc) phase of  $\text{CoPt}_3$ . The  $\text{CoPt}_3$  peaks slightly shift towards higher angles as the cobalt content increases (**Figure 7a**), suggesting the dissolution of Co in the fcc- $\text{CoPt}_3$  lattice. A crystallite size of  $5 \pm 1$  nm was determined using the Scherrer's formula, as expected from the nanocrystalline nature of the films. The hexagonal close-packed (hcp) phase of Co is detected in the diffraction patterns of the Co–Pt films prepared from Bath 2, in agreement with their higher cobalt content (**Figure 7b**). A shift of  $0.13^\circ$  toward lower angles is observed on the hcp-Co (100) peaks' position for films with

75 at.% and 85 at.% Co (red and blue curves, respectively) compared to the film with 58 at.% Co (black curve), proving that Pt is dissolved in the hcp-Co lattice. The films prepared from Bath 3 were structurally similar to those obtained from Bath 2 (**Figure 7c**), although some differences in texture were noticed. In particular, the  $I_{(100)}/I_{(101)}$  peak intensity ratio decreased as the cobalt content in the deposits increased (red and blue curves, **Figure 7c**). Compared to the films from Bath 1, deposits grown from Bath 3 showed narrower peaks, with a crystallite size of  $12 \pm 1$  nm. Considering that deposits from both baths (Bath 1 and 3) showed an evident and reproducible mesoporosity, this difference in the crystallite size values suggests that the formation of mesopores does not cause crystal refining. In other words, pore wall width is not correlated with crystal size, suggesting that each grown crystal is itself mesoporous.

### *3.5 Study of Pt(IV) complexes evolution with time*

To shed light on the evolution of chemical speciation of Pt(IV) during the equilibration time and its influence on the development of film mesostructure, UV-Vis spectroscopy of the  $[\text{PtCl}_6]^{2-}$  species in water was performed. For this purpose,  $\text{Na}_2\text{PtCl}_6$  was dissolved in water at a concentration of 0.0039 M and the dynamics of the resulting chloroaqua complexes was followed during several days (**Figure 8a**). Note that the concentration was increased by three times to better appreciate the features in the UV-Vis spectra. The obtained UV-Vis spectra at 0 days (black curve) showed a shoulder at 366 nm and a small peak at 455 nm which correspond to singlet and triplet ligand-field bands, respectively, as reported in previous works [25,26]. As shown in **Figure 8a**, a decrease of both peaks' intensity is observed over time, suggesting a decrease of the amount of chloro complexes ( $[\text{PtCl}_6]^{2-}$ ) in solution by the progressive exchange of  $\text{Cl}^-$  and  $\text{OH}^-$  ligands. This scenario is

schematically depicted in **Figure 8b**. During the equilibration time, Cl anions from  $[\text{PtCl}_6]^{2-}$  complex are exchanged by  $\text{OH}^-$  groups from the water molecules, resulting in the formation of  $[\text{PtCl}_{6-x}(\text{OH})_x]^{2-}$  complexes. This causes an increase of the concentration of  $\text{H}^+$  in solution, which in turn causes the pH to acidify (from 3.3 to 2.6), as experimentally observed (**Figure S1a,c and d**). This exchange between  $\text{Cl}^-$  and  $\text{OH}^-$  groups has been reported previously, where the dissociation of  $[\text{PtCl}_6]^{2-}$  is expected to be completed up to two Cl ligands [27]. Therefore, the equilibration time introduced during electrolyte preparation serves to increase the concentration of  $[\text{PtCl}_{6-x}(\text{OH})_x]^{2-}$  complexes.

Above its c.m.c., Pluronic P-123 forms micelles in water. The core of the micelles is made of the PPO block and the shell is made of PEO units. During the electrodeposition process, the Pt(IV) species coordinate to the shell of the P-123 micelle assemblies (**Figure 1**). The extent and strength of this coordination is critical for the development of mesoporosity in the deposits. Considering that the equilibration time promotes the formation of Pt(IV) chloroaqua complexes ( $[\text{PtCl}_{6-x}(\text{OH})_x]^{2-}$ ), it is conjectured that the  $\text{OH}^-$  groups from  $[\text{PtCl}_{6-x}(\text{OH})_x]^{2-}$  complex show higher affinity with the OH groups from the PEO block than  $\text{Cl}^-$  anions. A more efficient coordination between Pt(IV) and the PEO group of P-123 is thus expected for Baths 1, 3 and 4 than for Bath 2, thereby ensuring the correct, and importantly, reproducible formation of a long-range order mesoporosity in the films. Moreover, the observed changes on the UV-Vis spectra showed that 2 days of equilibration time seemed enough to secure the presence of a large concentration of  $[\text{PtCl}_{6-x}(\text{OH})_x]^{2-}$  complexes in solution. Indeed, deposits obtained with 2 days of equilibration time showed a flat morphology and mesoporosity analogous to the films prepared using 10 days of equilibration time (**Figure S6**). This result indicated that 2-day storage is also adequate for the correct formation of a mesoporous network in Co-Pt.



#### 4. Conclusions

The impact of electrolyte processing over the mesostructure of Co–Pt films grown from an aqueous solution containing P-123 micelle assemblies is unraveled. Prior dissolution of the Pt salt (or the Pt salt + P-123) in water and storage of the resulting solution before the P-123 amphiphilic surfactant and the Co salt (or the Co salt) are added decisively impacts the reproducibility of the mesostructure formation. To ensure the formation of highly mesoporous films, storage of the Pt(IV) solution (or the Pt(IV) + P-123 solution) for a few days (2–10) is recommended. In contrast, deposits grown from freshly prepared baths were usually non-mesostructured, thus suggesting that the factors involving the development of mesoporosity were uncontrolled. The parametric analysis of films obtained from various baths having exactly the same formulation and pH but subject to a different electrolyte processing prior to electrodeposition clearly indicated that the Co/Pt ratio in the films could not explain why mesoporosity consistently developed in some cases and not in others. UV-Vis monitoring of a Pt(IV) aqueous solution allowed us to verify that the formation of chloroaqua complexes during the storage period was key for the development of mesoporosity. We suggest that the higher affinity of the  $[\text{PtCl}_{6-x}(\text{OH})_x]^{2-}$  complexes with the PEO groups of the P-123 micelle assemblies warrants the formation of compositionally homogeneous deposits with a reproducible mesoporosity. Our research highlights the significance of electrolyte processing in the electrosynthesis of mesoporous Co-Pt films and suggests that a similar protocol to guarantee the formation of mesoporous films with a high degree of reproducibility should be adopted in other systems.

## **Acknowledgements**

This work was funded by the Spanish Government (Project MAT2017-86357-C3-1-R and associated FEDER), the Generalitat de Catalunya (2017-SGR-292), and the European Research Council (SPIN-PORICS 2014-Consolidator Grant, Agreement nº 648454).

## References

- 1 S. C. Warren and U. Wiesner, *Pure Appl. Chem.*, 2009, **81**, 73–84.
- 2 M. T. Y. Paul and B. D. Gates, *Sci. Rep.*, 2019, **9**, 4161.
- 3 V. Malgras, H. Ataee-Esfahani, H. Wang, B. Jiang, C. Li, K. C. W. Wu, J. H. Kim and Y. Yamauchi, *Adv. Mater.*, 2016, **28**, 993–1010.
- 4 J. M. Elliott, P. R. Birkin, P. N. Bartlett and G. S. Attard, *Langmuir*, 1999, **15**, 7411–7415.
- 5 H. Wang, L. Wang, T. Sato, Y. Sakamoto, S. Tominaka, K. Miyasaka, N. Miyamoto, Y. Nemoto, O. Terasaki and Y. Yamauchi, *Chem. Mater.*, 2012, **24**, 1591–1598.
- 6 M. Iqbal, C. Li, K. Wood, B. Jiang, T. Takei, Ö. Dag, D. Baba, A. S. Nugraha, T. Asahi, A. E. Whitten, M. S. A. Hossain, V. Malgras and Y. Yamauchi, *Chem. Mater.*, 2017, **29**, 6405–6413.
- 7 B. Jiang, C. Li, H. Qian, M. S. A. Hossain, V. Malgras and Y. Yamauchi, *Angew. Chemie - Int. Ed.*, 2017, **56**, 7836–7841.
- 8 H. Wang, M. Imura, Y. Nemoto, L. Wang, H. Y. Jeong, T. Yokoshima, O. Terasaki and Y. Yamauchi, *Chem. - A Eur. J.*, 2012, **18**, 13142–13148.
- 9 C. Li, H. Wang and Y. Yamauchi, *Chem. - A Eur. J.*, 2013, **19**, 2242–2246.
- 10 K. Eiler, S. Suriñach, J. Sort and E. Pellicer, *Appl. Catal. B Environ.*, 2020, **265**, 118597.
- 11 E. Isarain-Chávez, M. D. Baró, C. Alcantara, S. Pané, J. Sort and E. Pellicer, *ChemSusChem*, 2018, **11**, 367–375.
- 12 C. Navarro-Senent, J. Fornell, E. Isarain-Chávez, A. Quintana, E. Menéndez, M. Foerster, L. Aballe, E. Weschke, J. Nogués, E. Pellicer and J. Sort, *ACS Appl. Mater. Interfaces*, 2018, **10**, 44897–44905.
- 13 M. Bechelany, A. Abou Chaaya, F. Frances, O. Akdim, D. Cot, U. B. Demirci and P. Miele, *J. Mater. Chem. A*, 2013, **1**, 2133–2138.

- 14 J. Zhang, S. Agramunt-Puig, N. Del-Valle, C. Navau, M. D. Baró, S. Estradé, F. Peiró, S. Pané, B. J. Nelson, A. Sanchez, J. Nogués, E. Pellicer and J. Sort, *ACS Appl. Mater. Interfaces*, 2016, **8**, 4109–4117.
- 15 A. H. Whitehead, J. M. Elliott, J. R. Owen and G. S. Attard, *Chem. Commun.*, 1999, 331–332.
- 16 A. N. Correia and S. A. S. Machado, *Electrochim. Acta*, 2000, **45**, 1733–1740.
- 17 A. Nicolenco, N. Tsyntsar and H. Cesiulis, *J. Electrochem. Soc.*, 2017, **164**, D590–D596.
- 18 A. Serrà, E. Gómez and E. Vallés, *Int. J. Hydrogen Energy*, 2015, **40**, 8062–8070.
- 19 N. Wang and D. P. Arnold, *IEEE Trans. Magn*, 2008, **44**, 3969–3972.
- 20 G. Wanka, H. Hoffmann and W. Ulbricht, *Macromolecules*, 1994, **27**, 4145–4159.
- 21 S. Grau, M. Montiel, E. Gómez and E. Vallés, *Electrochim. Acta*, 2019, **109**, 187–194.
- 22 E. Pellicer, S. Pané, K. M. Sivaraman, O. Ergeneman, S. Suriñach, M. D. Baró, B. J. Nelson and J. Sort, *Mater. Chem. Phys.*, 2011, **130**, 1380–1386.
- 23 G. Pattanaik and G. Zangari, *J. Electrochem. Soc.*, 2006, **156**, C6–C10.
- 24 C. Wang, D. Chen and X. Jiao, *Sci. Technol. Adv. Mater.*, 2009, **10**, 023001–023012.
- 25 L. E. Cox, D. G. Peters and E. L. Wehry, *J. Inorg. Nucl. Chem.*, 1972, **34**, 297–305.
- 26 A. Goursot, E. Penigault and H. Chermette, *Chem. Phys. Lett.*, 1983, **97**, 215–220.
- 27 Antos George J. and Aitani Abdullah M., *Catalytic Naphtha Reforming, Revised and Expanded*, 2004.

## Figure captions

**Figure 1.** Scheme of the micelle-assisted electrodeposition of mesoporous Co–Pt thin films. Step 1: P-123 micelles form spontaneously in the electrolyte. Step 2: the metal ions coordinate to the outer hydrophilic shell of the P-123 micelles. Step 3: the metallic ions reduce at the cathode by virtue of the applied potential. Step 4: P-123 surfactant is removed, leaving the mesoporous metallic Co-Pt film behind.

**Figure 2.** CV curves recorded under stationary conditions at  $50 \text{ mV s}^{-1}$  from Bath 1 (black curve) and Bath 2 (blue curve) on vitreous carbon.

**Figure 3.** CV curves recorded under stationary conditions at  $50 \text{ mV s}^{-1}$  from Bath 1 (black curve) and Bath 3 (green curve) on vitreous carbon. 'eq. time' stands for equilibration time, the concentration of  $\text{CoCl}_2$  in each bath is indicated.

**Figure 4.** Representative FE-SEM images of the Co–Pt films electrodeposited from Bath 1 at (a)  $-0.9$  (b)  $-1.0$  and (c)  $-1.1 \text{ V}$  during  $600 \text{ s}$ . (d-f) Corresponding pore size distribution histograms.

**Figure 5.** Representative FE-SEM images of the Co–Pt films electrodeposited from Bath 2 at (a)  $-1.2$  (b)  $-1.3$  and (c)  $-1.4 \text{ V}$  during  $600 \text{ s}$ .

**Figure 6.** Representative FE-SEM images of the Co–Pt films electrodeposited from Bath 3 at (a)  $-0.9$  (b)  $-1.0$  and (c)  $-1.1 \text{ V}$  during  $600 \text{ s}$ .

**Figure 7.** XRD of the Co–Pt films electrodeposited from (a) Bath 1 at  $-0.9$  (black),  $-1.0$  (red) and  $-1.1 \text{ V}$  (blue), (b) Bath 2 at  $-1.1$  (black),  $-1.2$  (red) and  $-1.3 \text{ V}$  (blue) and (c) Bath 3 at  $-0.9$  (black),

–1.0 (red) and –1.1 V (blue). The fcc-Cu signal originates from the Cu seed-layer of the substrate, ‘eq. time’ stands for equilibration time.

**Figure 8.** (a) Time dependent evolution of UV-Vis absorbance spectra of Pt(IV) complexes in water (0.0039 M) and (b) Scheme of ligand exchange taking place during the equilibration time.

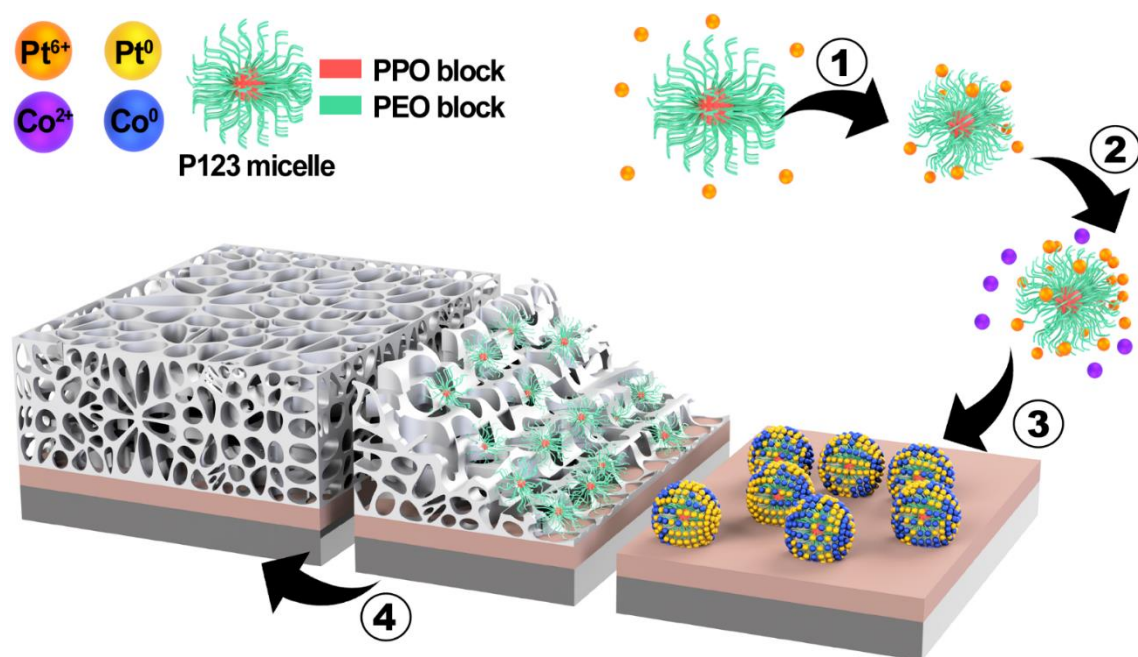


Figure 1

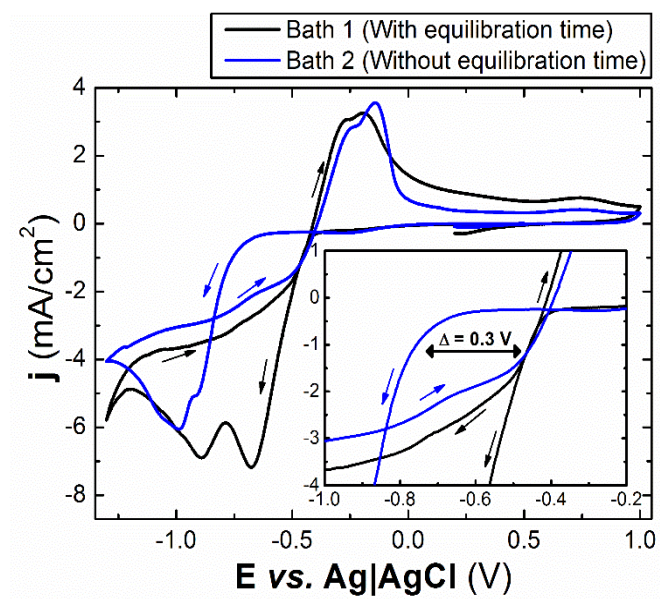


Figure 2



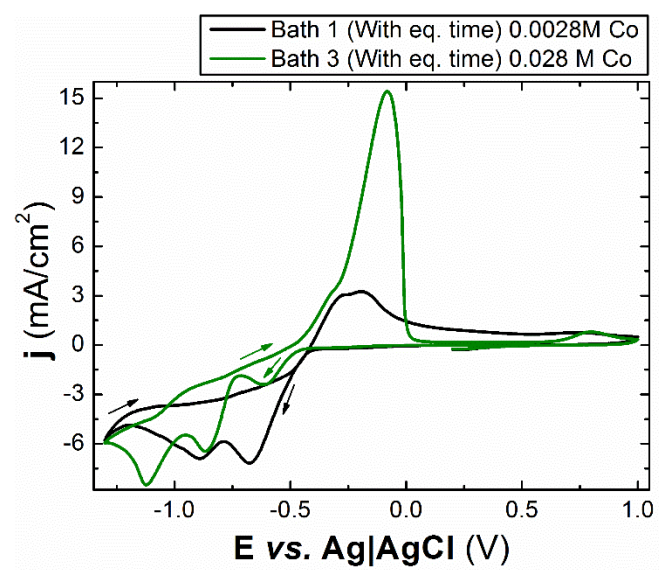


Figure 3

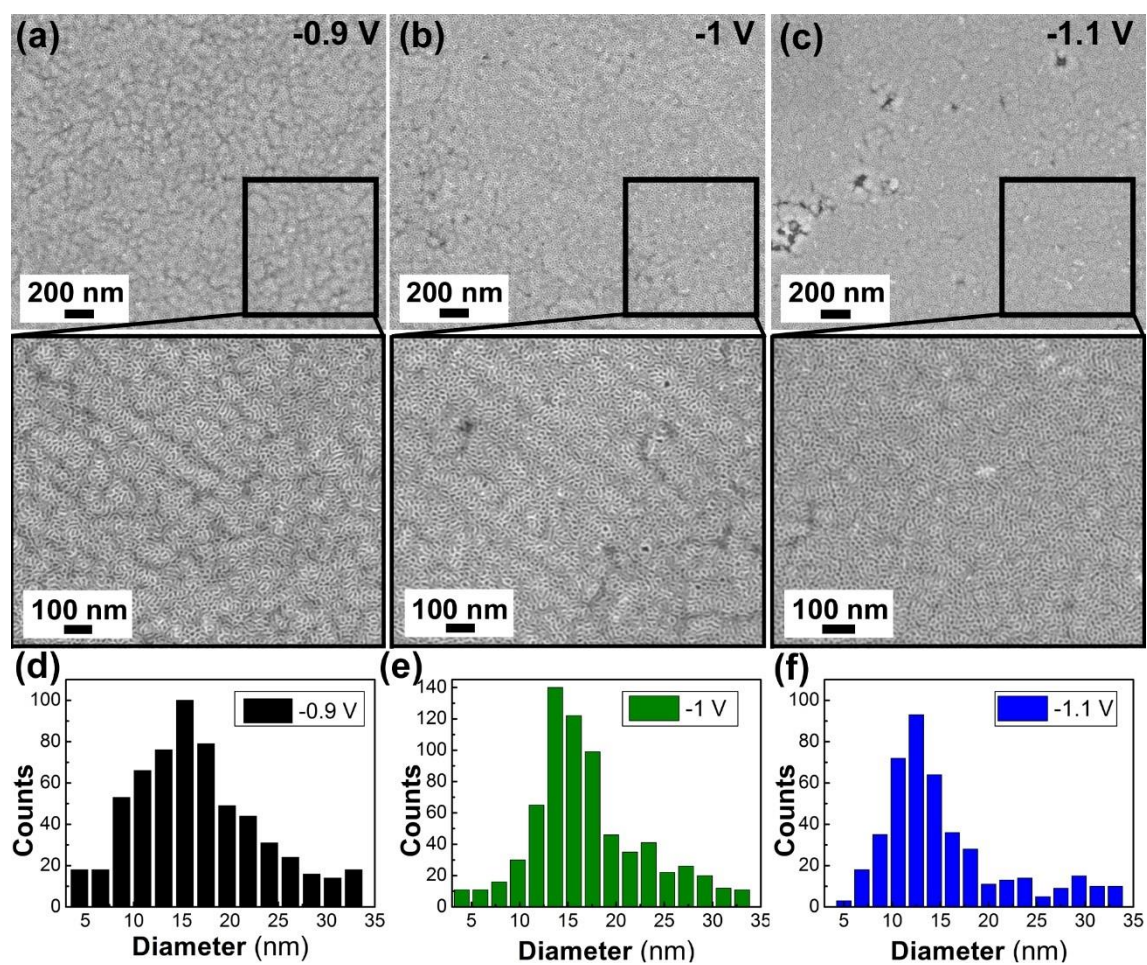


Figure 4

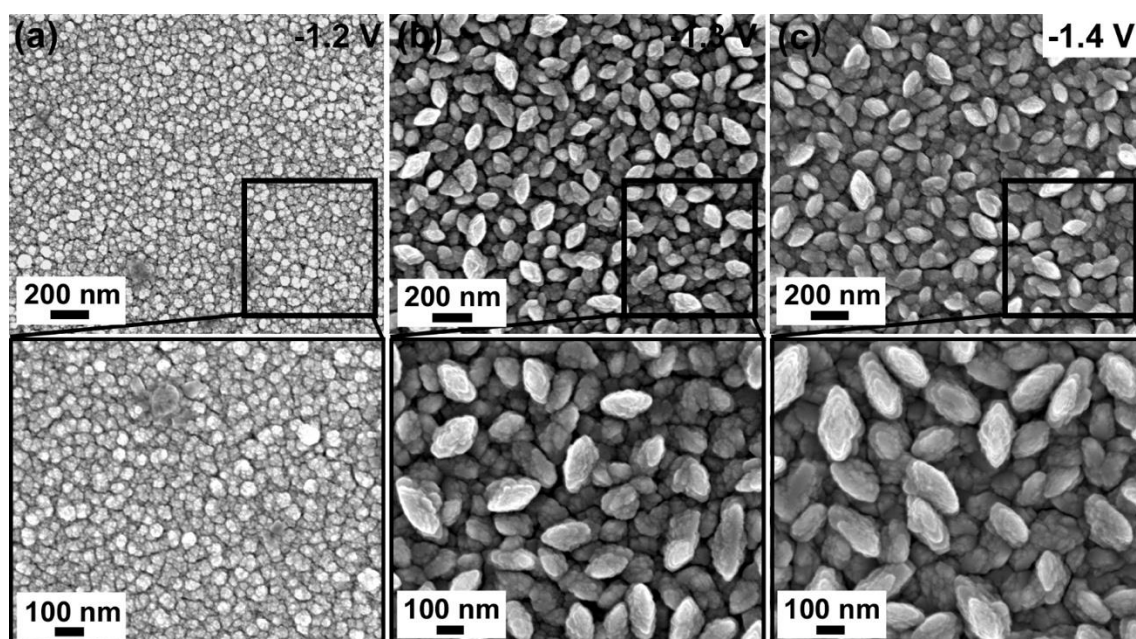


Figure 5

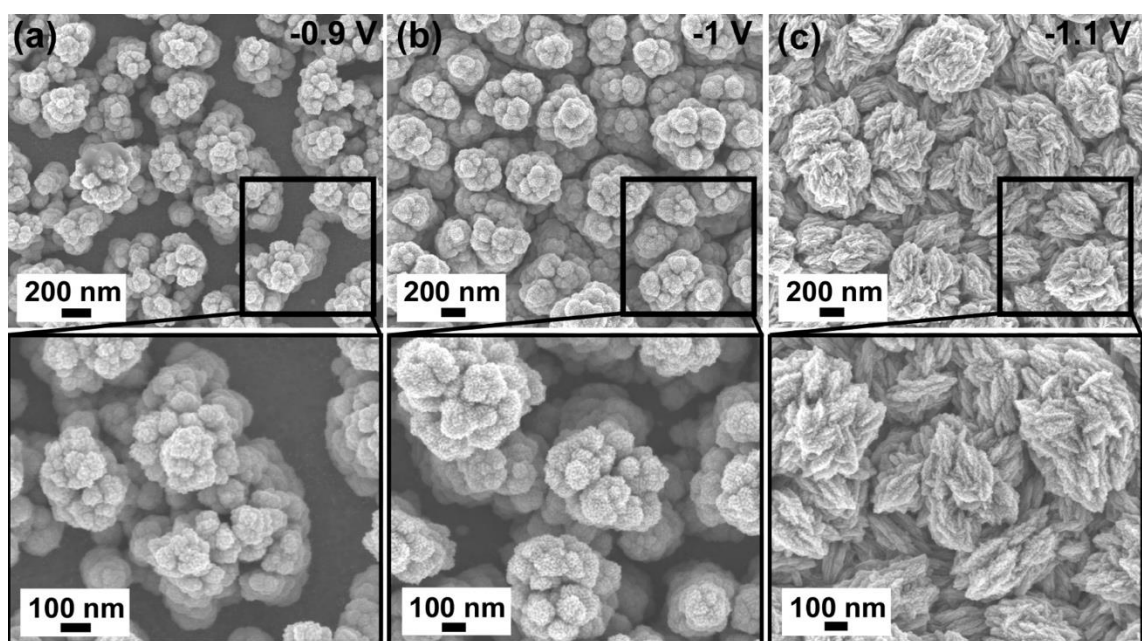


Figure 6

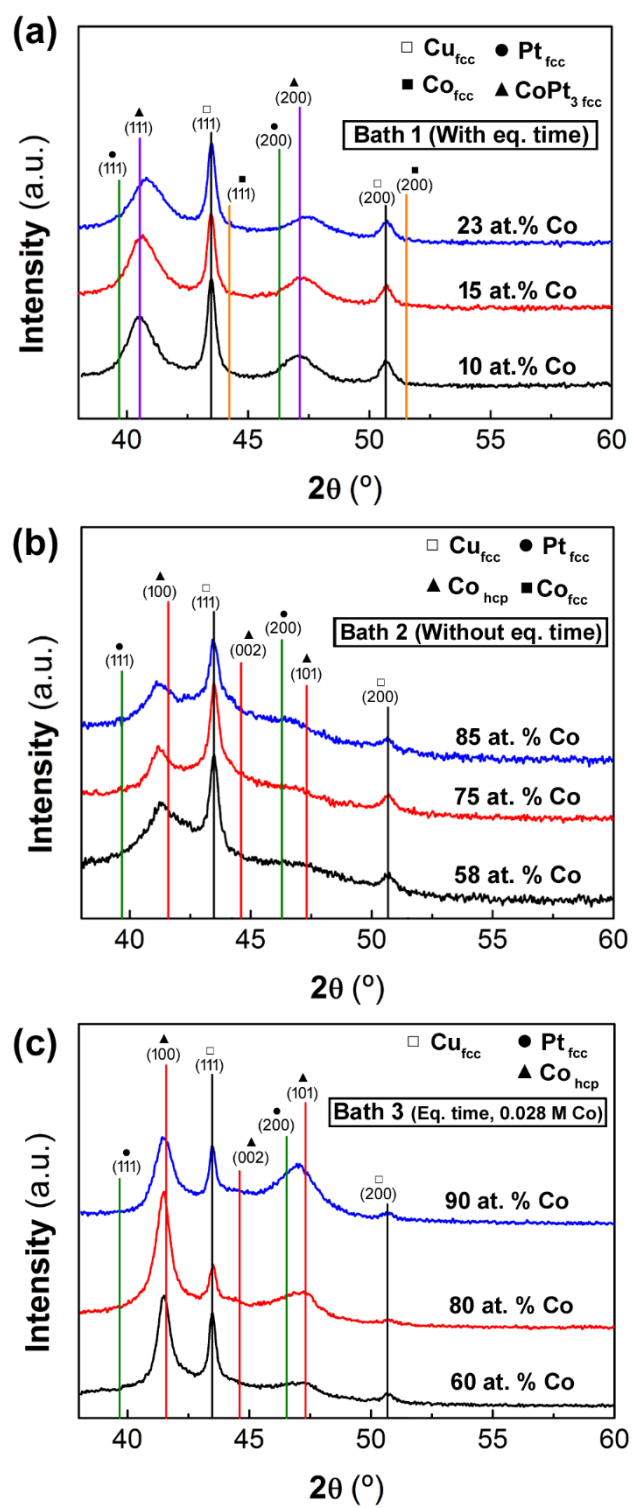


Figure 7

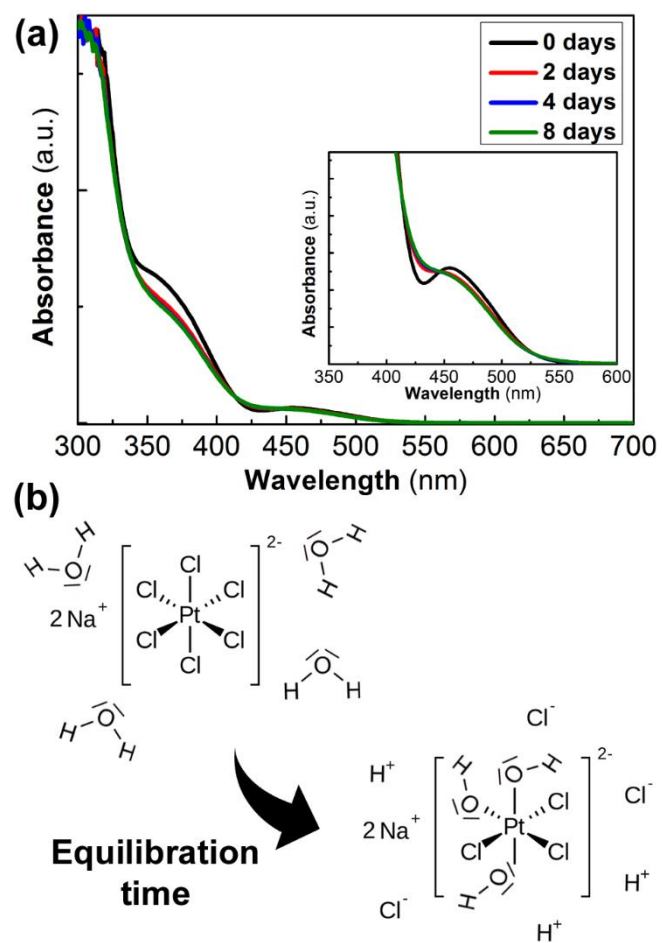











Figure 8

**Table 1.** Bath composition and electrodeposition conditions utilized in Baths 1-4. In the equilibration time row, the indicated species were dissolved in water and the solution left 10 days at room temperature before  $\text{CoCl}_2$  + P-123 (Baths 1 and 3) or  $\text{CoCl}_2$  only (Bath 4) were added.

Bath	1	2	3	4
Equilibration time (10 days)	$\text{Na}_2\text{PtCl}_6$	–	$\text{Na}_2\text{PtCl}_6$	$\text{Na}_2\text{PtCl}_6$ + P-123
<b>Bath composition and electrodeposition conditions:</b>				
$[\text{Na}_2\text{PtCl}_6] / \text{M}$	0.0013			
$[\text{CoCl}_2] / \text{M}$	0.0028	0.0028	0.028	0.0028
$[\text{P-123}] / \text{mg mL}^{-1}$	1 (= 1 wt %)			
pH	2.3			
$T / ^\circ\text{C}$	25			
$E / \text{V}$	–0.9, –1.0, –1.1	–1.2, –1.3, –1.4	–0.9, –1.0, –1.1	–0.9, –1.0, –1.1
$t / \text{s}$	600			

**Table 2.** Cobalt content (in at.%) in the Co–Pt films deposited from the various baths and photos of the films. The orange-like colour corresponds to the Cu seed-layer, which was used for the electrical connection during electrodeposition. The light grey or dark grey part corresponds to the Co–Pt film covering the remaining Cu surface.

Bath	Co at. %					
	–0.9 V	–1 V	–1.1 V	–0.9 V	–1 V	–1.1 V
<b>1</b>	10	15	23			
<b>3</b>	60	80	90			
<b>4</b>	15	20	28			
Bath	Co at. %					
	–1.2 V	–1.3 V	–1.4 V	–1.2 V	–1.3 V	–1.4 V
<b>2</b>	58	75	85	